applied optics

Dynamic wavefront distortion in resonant scanners

VYAS AKONDI,* BARTLOMIEJ KOWALSKI, AND ALFREDO DUBRA

Byers Eye Institute, Stanford University, Palo Alto, California 94303, USA
*Corresponding author: vakondi@stanford.edu

Received 22 September 2021; accepted 13 November 2021; posted 19 November 2021 (Doc. ID 443972); published 13 December 2021

Dynamic mirror deformation can substantially degrade the performance of optical instruments using resonant scanners. Here, we evaluate two scanners with resonant frequencies > 12 kHz with low dynamic distortion. First, we tested an existing galvanometric motor with a novel, to the best of our knowledge, mirror substrate material, silicon carbide, which resonates at 13.8 kHz. This material is stiffer than conventional optical glasses and has lower manufacturing toxicity than beryllium, the stiffest material currently used for this application. Then, we tested a biaxial microelectromechanical (MEMS) scanner with the resonant axis operating at 29.4 kHz. Dynamic deformation measurements show that wavefront aberrations in the galvanometric scanner are dominated by linear oblique astigmatism (90%), while wavefront aberrations in the MEMS scanner are dominated by horizontal coma (30%) and oblique trefoil (27%). In both scanners, distortion amplitude increases linearly with deflection angle, yielding diffraction-limited performance over half of the maximum possible deflection for wavelengths longer than 450 nm and over the full deflection range for wavelengths above 850 nm. Diffraction-limited performance for shorter wavelengths or over larger fractions of the deflection range can be achieved by reducing the beam diameter at the mirror surface. The small dynamic distortion of the MEMS scanner offers a promising alternative to galvanometric resonant scanners with desirable but currently unattainably high resonant frequencies. © 2021 Optica Publishing Group under the terms of the Optica Open Access Publishing Agreement

https://doi.org/10.1364/AO.443972

1. INTRODUCTION

Optical resonant scanners are widely used across applications as diverse as intraoperative imaging [1], microscopy [2–4], retinal imaging [5–7], optical coherence tomography [8,9], underwater imaging [10], flow cytometry [11], and high-resolution printing [12,13]. The mirrors of resonant scanners suffer from dynamic distortions caused by the linear variation in torque with deflection angle [14,15]. This distortion can be estimated using finite-element analysis models [16–19], or measured, as has been demonstrated, using stroboscopic interferometry [16,20–22] and Shack–Hartmann wavefront sensing (SHWS) [20,23]. Using a custom SHWS, we recently showed that such dynamic distortion in a 15.1 kHz resonant galvanometric scanner with a Clearceram-Z (Ohara Corporation, Rancho Santa Margarita, CA, U.S.) mirror substrate held at only one end was dominated by oblique astigmatism that could result in up to a 90% Strehl ratio degradation at 680 nm [23]. This material has mechanical properties similar to those of the most widely used optical glasses. In the same study, we showed that a similar scanner with a 2× thicker beryllium substrate operating at 7.9 kHz provided diffraction-limited imaging (i.e., a Strehl ratio >0.8) at the same wavelength. Unfortunately, the highest frequency of commercially available beryllium scanners is only 12 kHz, which is limiting for imaging of live and/or moving samples/objects. Therefore, we set out to explore two new avenues to deliver high-frequency resonant scanners with low dynamic distortion, and comparable or higher Lagrange invariants (i.e., product of the maximum deflection angle and mirror aperture size) than those of current resonant scanners.

First, we evaluated an off-the-shelf scanner motor (SC-30; Electro-optical Products Corporation, EOPC; Ridgewood, NY, U.S.) with a custom silicon carbide (SiC) mirror by OptoSic (Mersen Deutschland Holding GmbH & Co. KG, München, Germany) resonating at 13.8 kHz. This relatively new optical material was chosen because of its specific stiffness (or specific modulus) of 133×10^6 m^2/s^2, which compares favorably to the 33×10^6 m^2/s^2 of BK7 and fused silica, which are both widely used optical glasses. Importantly, SiC composites [24–27] offer a potentially lower toxicity alternative [28] to beryllium, which has a specific stiffness $\sim 160 \times 10^6$ m^2/s^2 and, which during the machining and polishing process produces dust known to pose a serious health hazard [29].

Then, we evaluated a new type of microelectromechanical systems (MEMS) bidirectional optical scanner (S13989-01H; Hamamatsu, Hamamatsu-City, Japan) with the resonant axis operating at 29.4 kHz. MEMS optical scanners are appealing due to their smaller size and lower power consumption than

galvanometric and rotating polygon scanners. The smaller moment of inertia of MEMS mirrors is also appealing due to their higher resonant frequencies [17,30–32] and/or higher Lagrange invariants [22,33]. Because of these advantages, resonant optical MEMS scanners are being increasingly used in microscopy [34–43], high-resolution displays [17,44–46], automotive vehicles [47–49], barcode reading [32,50,51], and biometrics [52,53], among other applications. The next section describes the experimental setup and the calculation of wavefront metrics, which is followed by results and a brief summary section.

2. METHOD

A custom SHWS with an EXi Aqua camera (Teledyne Qimaging, Surrey, BC, Canada) and a lenslet array with 203 µm pitch, 9.35 mm geometrical focal length, and refocused to account for focal shift [54] was used to measure the dynamic distortions of the scanning mirrors. Light from a 5 mW, 680 nm superluminescent diode from Superlum (S-680-G-I-5, Carrigtwohill, Co. Cork, Ireland), was collimated and passed through a linear polarizer to illuminate the double-pass optical setup shown in Fig. 1 for testing the galvanometric

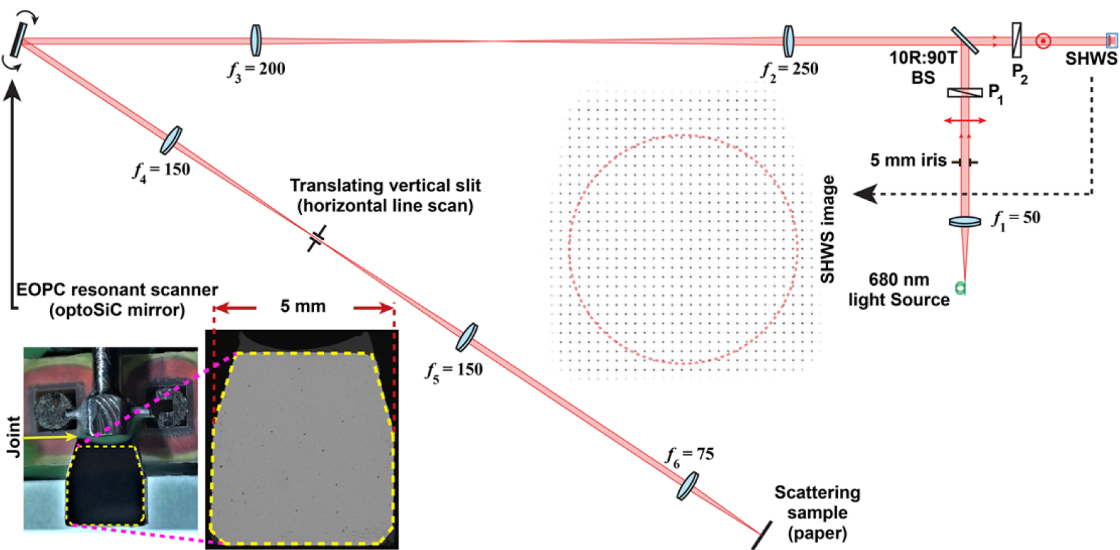

Fig. 1. Testbed used for measuring dynamic wavefront distortion in a galvanometric resonant scanner with a SiC mirror. In this diagram, BS is a beam splitter, f_i represents focal length of an achromatic lens in millimeters, and P_j denotes a linear polarizer. A red dotted line shows a 4 mm pupil over a SHWS image. The bottom left panels show the mirror in its mount and a magnified inset.

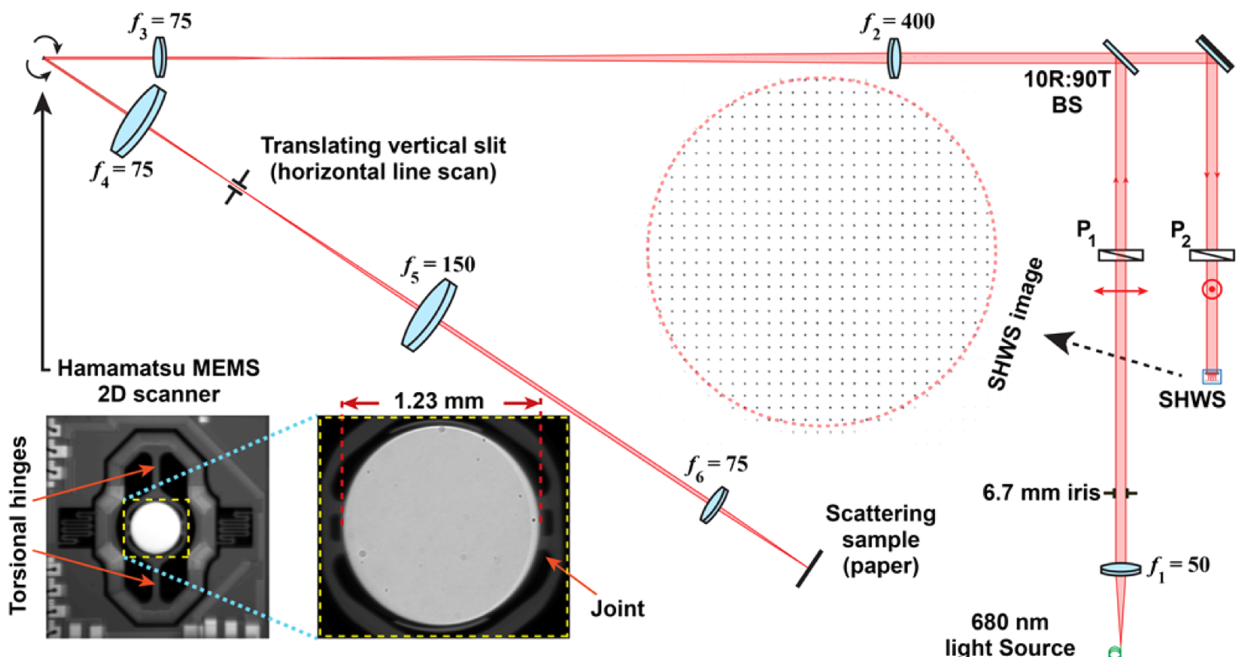

Fig. 2. Testbed used for measuring dynamic wavefront distortion in a MEMS resonant scanner. In this diagram, BS is a beam splitter, f_i represents focal length of an achromatic lens in millimeters, and P_j denotes a linear polarizer. A red dotted line shows a 1.2 mm pupil over a SHWS image. The bottom left panels show the mirror in its mount and a magnified inset.

resonant scanner. This setup was slightly modified as per Fig. 2 to test the MEMS scanner, which has a substantially smaller mirror. In short, the optical setups consist of two afocal relays and lens with a piece of paper in its focal plane, with the only significant difference between the setups being the magnification of the beam at the resonant scanner plane.

The scattering of the focused light that is scanned across the paper effectively erases the wavefront of the light's first pass through the optical setup. In this way, the descanned beam at the SHWS only contains the wavefront aberrations of the return path (i.e., between the paper and the SHWS). A 400 μm wide slit, slightly tilted to eliminate undesired reflections, was placed in a plane conjugate to the paper to ensure that the SHWS only collected light when the scanner is at a desired deflection angle. The wavefront distortions reported below are, therefore, the wavefront averaged over multiple scanner oscillations as the beam crosses the slit. The width of the slit was chosen as an arbitrary compromise between sampling the desired location more precisely (i.e., narrower slit) and acceptable signal-to-noise ratio (i.e., wider slit). A linear polarizer in front of the SHWS was oriented to mitigate undesired backreflections from the lenses.

SHWS images were captured at scanner deflection between 0° and 2.3° for the 13.8 kHz scanner and 0° and 12.2° for the 29.4 kHz scanner (with the nonresonant axis unpowered). Data were not captured for negative angles due to the symmetry expected from the approximate linear nature of the wavefront distortion, both from theory [14] and experimental results [23]. The static wavefront distortions due to the optical elements in the setups and the scanner mirrors themselves were measured by capturing additional SHWS images with the resonant scanners manually rotated about their pivot point with the scan amplitude set to its minimum value (0.25 mA driving current for the MEMS scanner and 50 mV for the galvanometric scanner). Speckle averaging, achieved by these small amplitude oscillations, erases the wavefront of the light's first pass through the optics [55].

The centroids of the SHWS lenslet images were determined using an iterative fractional centroiding algorithm [23] with a final search box width equal to that of the diffraction-limited lenslet image central lobe. Centroid displacements due to dynamic wavefront distortions were calculated by subtracting the centroids of the images captured with static aberrations alone from those of images captured with static plus dynamic aberrations. The local wavefront slope at each lenslet center

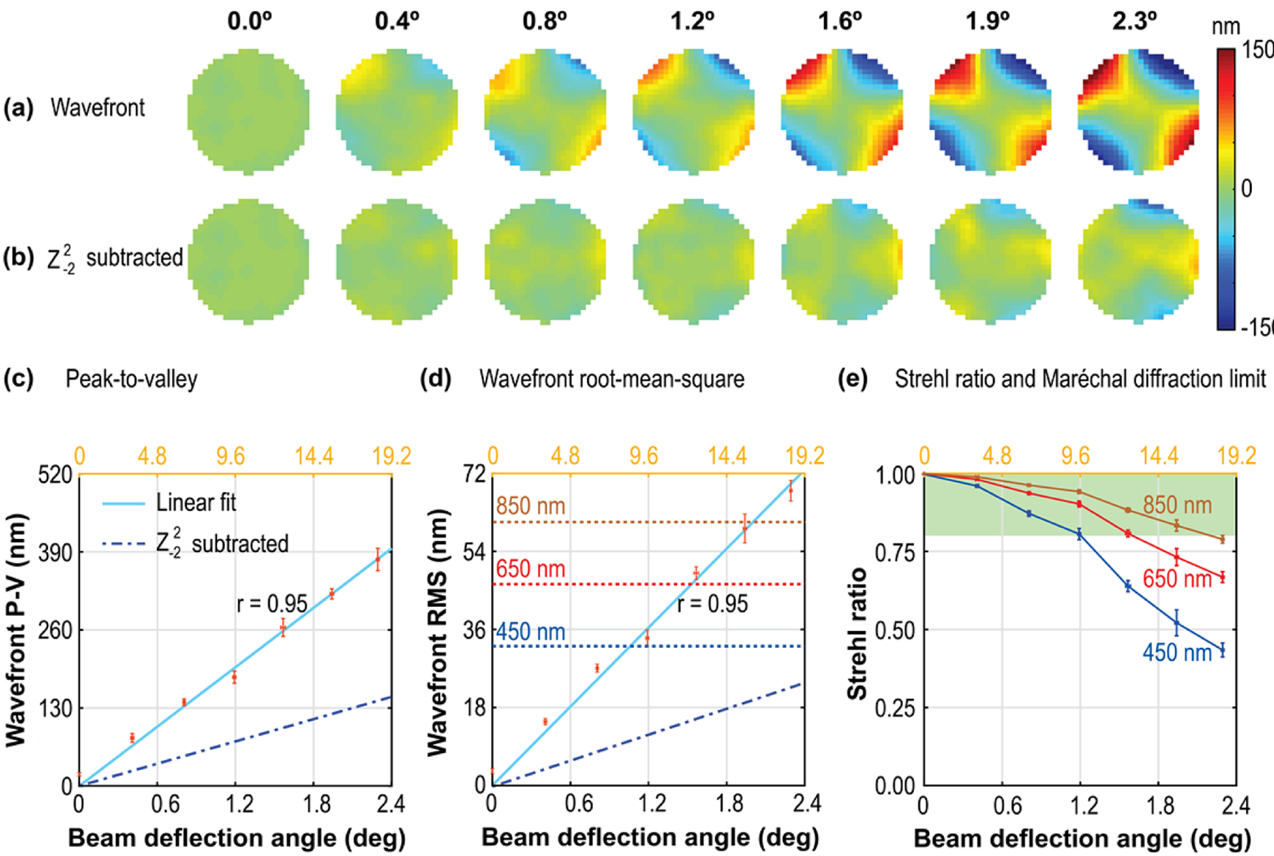

Fig. 3. Dynamic wavefront distortions at various deflection angles in a galvanometric resonant scanner with a SiC mirror oscillating at 13.8 kHz and over a 4 mm clear aperture diameter. (a) Full wavefront, and (b) after oblique astigmatism subtraction; (c) and (d) show the linear increase of wavefront P-V and RMS with beam deflection angle. The dotted lines parallel to the x axis in (d) represent diffraction-limited RMS for the corresponding wavelengths. The Strehl ratio as a function of the beam deflection angle at 450, 650 and 850 nm wavelengths is shown in (e), and the green shaded region satisfies Maréchal diffraction-limited performance. The values along the top horizontal axes in light orange denote the Lagrange invariant (product of maximum peak-to-peak beam deflection angle and beam diameter) in units of millimeters/degrees to facilitate performance comparison with other scanners.

was calculated as the ratio of the centroid displacements and the lenslet focal length. The wavefronts were estimated over a circular SHWS camera region (see dotted red circles in Figs. 1 and 2), using a least-squares fitting of Zernike polynomial gradients up to the 15th order, accounting for the averaging over each lenslet [56]. The results were verified with zonal wavefront integration following the slope geometry of Southwell [57]. The wavefront root-mean-square (RMS) reproducibility error was found to be lower than 5.1 nm. The errors due to SHWS sampling and illumination nonuniformities [58] are expected to be lower than 0.1% and 0.6%, respectively, for each of the Zernike polynomials of interest. The discrete Fourier transform was used to evaluate the point spread function (PSF), assuming a uniformly illuminated circular pupil. The corresponding Strehl ratios were then estimated from the on-axis intensity normalized to that of an aberration-free beam through the same pupil [59].

3. RESULTS

Dynamic wavefront distortion for the 13.8 kHz scanner, shown in Fig. 3(a), is dominated by oblique astigmatism (90%), followed by vertical astigmatism (6%) and oblique trefoil (3%). These aberrations are consistent with those seen in resonant scanners in which mirrors are attached to the motor only on one side [23]. The plots in Figs. 3(c)–3(e) reveal that, as expected, the wavefront peak-to-valley (P-V) and RMS are directly proportional to the angular deflection, and the Strehl ratio drops for larger beam deflection angles. If the linear oblique astigmatism were compensated, for example, as proposed by Huang and Dubra [60], the residual wavefronts, shown in Fig. 3(b), and their P-V and RMS at 2.3° would be reduced to 143 from 377 nm and to 22 from 68 nm, respectively. This correction would result in diffraction-limited performance (i.e., RMS < 1/14 wave or Strehl ratio >0.8) at 450, 650, and 850 nm over beam deflection angles equal or smaller than 1°, 1.5°, and 2°, respectively, as can be seen in Figs. 3(d) and 3(e).

The dynamic wavefront distortion of the 29.4 kHz MEMS resonant scanner, measured over the clear aperture, which includes nearly 98% of the mirror's diameter (1.2 mm), is shown in Fig. 4 for various deflection angles. For these wavefronts, the mean RMS and mean P-V at 12.2° deflection, are 39 and 330 nm, respectively, dominated by Zernike horizontal coma (30%) and oblique trefoil (27%). The dominance of these aberrations is consistent with the fact that boundary conditions are imposed by the clamping of the scanner mirror at the top and bottom, which means that only aberrations described by Zernike polynomials with odd radial orders [61] can be present. Moreover, the vertical mirror symmetry means that only aberrations symmetric relative to the horizontal axis should be observed, (i.e., Zernike polynomials with positive azimuthal indices), which is also consistent with our data.

Extrapolation of the dynamic wavefront P-V to the scanner largest possible beam deflection angle (20°, not measured due to the limited numerical aperture of our optics) with a 1.2 mm pupil diameter, predicts a wavefront P-V of 485 nm, which is close to the manufacturer's 480 nm prediction from finite-element analysis shown in Fig. 5.

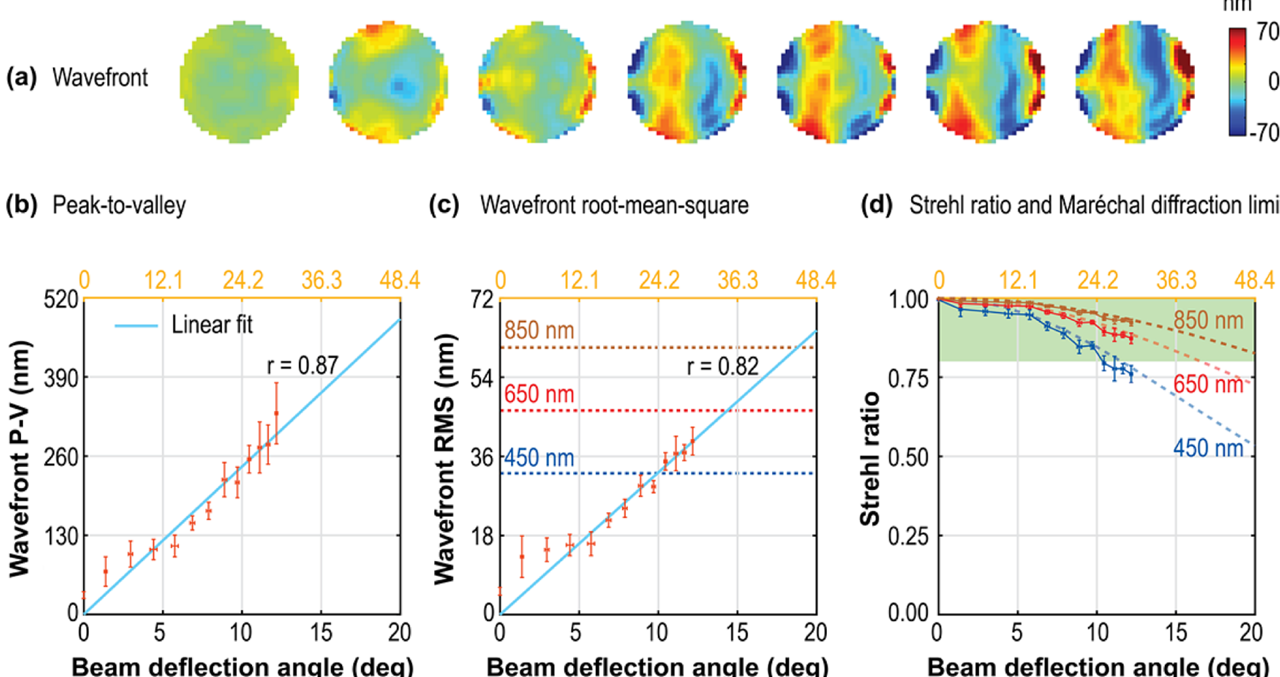

Fig. 4. (a) Dynamic wavefront distortions at various deflection angles in a MEMS resonant scanner oscillating at 29.4 kHz and over a 1.2 mm clear aperture diameter; (b) and (c) show the linear increase of wavefront P-V and RMS with beam deflection angle. The dotted lines parallel to the x axis in (c) represent Maréchal diffraction-limited RMS for the corresponding wavelengths. The Strehl ratio as a function of the beam deflection angle at 450, 650, and 850 nm wavelengths is shown in (d), and the green shaded region satisfies Maréchal diffraction-limited performance. The dotted lines in (d) represent extrapolated Strehl ratios. The values along the top horizontal axes in light orange denote the Lagrange invariant (product of maximum peak-to-peak beam deflection angle and beam diameter) in units of millimeters/degrees to facilitate performance comparison with other scanners.

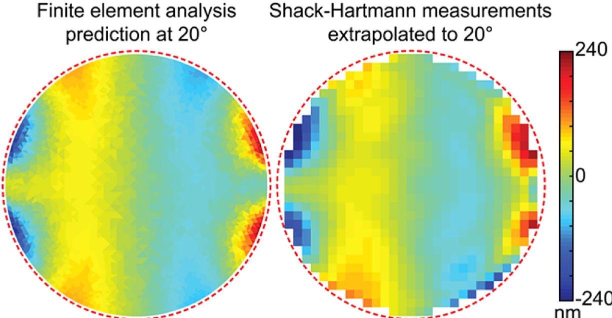

Fig. 5. Comparison of manufacturer's prediction through finite-element analysis of the dynamic wavefront deformation of the MEMS mirror (1.20 mm clear aperture diameter) resonating at 29.4 kHz and ±20° (left) against the corresponding extrapolated Shack–Hartmann wavefront sensor measurement (right). The dotted red circle has a diameter of 1.23 mm.

The wavefront RMS and Strehl ratio plots in Figs. 4(c) and 4(d) show that, assuming the absence of static aberrations, for wavelengths 850 nm and longer, the scanner is effectively diffraction-limited over its entire ± 20° deflection range and over its full clear aperture. For visible wavelengths, however, this is only the case for half of its dynamic range. This can be overcome, however, by using a narrower beam, as illustrated in Fig. 6, provided that the desired Lagrange invariant can still be achieved. For example, reducing the beam diameter to 80% of the clear aperture would reduce the wavefront RMS by 44%, increasing the Strehl ratio at 20° from 0.53 to 0.85 at 450 nm. Similarly, a reduction in the beam diameter at the 13.8 kHz galvanometric scanner operating from its clear aperture diameter from 4.0 to 3.0 mm (75%) would reduce the wavefront RMS by 47% and increase the Strehl ratio from 0.44 to 0.79, at a beam deflection angle of 2.3° and 450 nm wavelength.

4. SUMMARY

Despite the wide availability and use of mechanical resonant optical scanners, their dynamic distortion continues to limit their performance. This is critical for applications such as retinal imaging [6,7], which plays a significant role in the diagnosis and management of blinding conditions, as well as functional imaging of biological tissues and organs, such as the brain [62–64]. In order to advance these and other medical and scientific applications, mechanical scanners with higher resonant frequencies than those currently available and with low dynamic distortion are needed. This is because rapid scanning technologies that

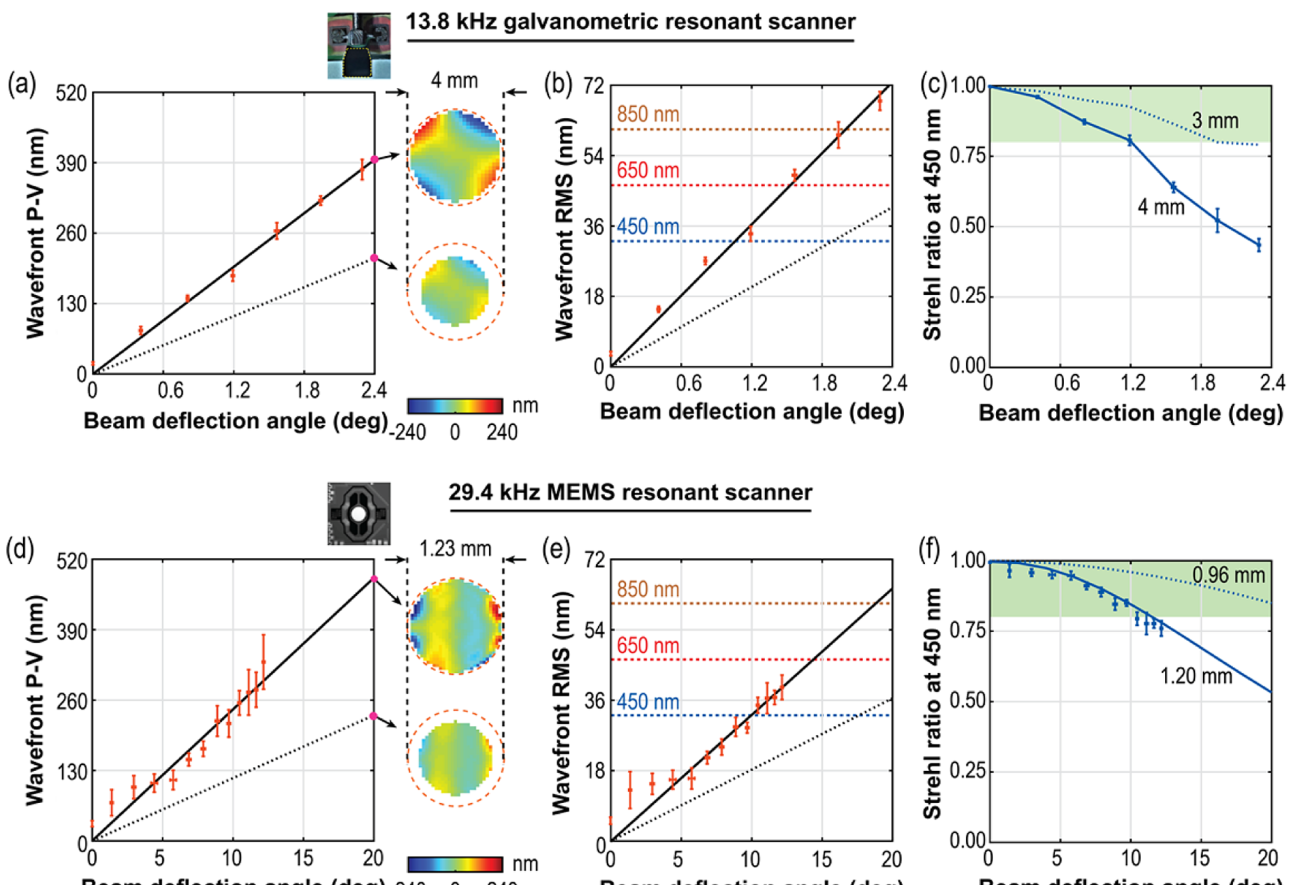

Fig. 6. Comparison of wavefront P-V, wavefront RMS, and Strehl ratio (450 nm), when using two different pupil sizes at the resonant scanner mirrors: 4 (solid lines) and 3 mm (dotted lines) for the 13.8 kHz galvanometric resonant scanner; and similarly, 1.20 (solid lines) and 0.96 mm (dotted lines) for the 29.4 kHz MEMS resonant scanner. The dotted lines parallel to the x axis in (b) and (e) represent Maréchal diffraction-limited RMS for the wavelengths shown and the green shaded region in (c) and (f) satisfies diffraction-limited performance. The solid and dotted lines in (c) represent lines joining data points, and those in (f) represent fitted and extrapolated Strehl ratio values.

exploit optical phenomena such as optoacoustic deflection, are wavelength- and/or polarization-dependent, and often dispersive. Mechanical deflection using metallic coating mirrors such as those used here, however, are achromatic, have negligible polarization-sensitivity, minimal dispersion, and are compatible with high optical powers. Hence, mechanical scanners will continue to be widely used for the foreseeable future.

Here, we evaluated two promising alternatives, one that could improve the performance of existing galvanometric resonant scanners by using mirror substrates made of novel materials such as SiC, and one that could altogether replace traditional galvanometric mirrors, which is the latest generation of MEMS optical scanners with double the maximum resonant frequencies than were previously possible. Our data show that the SiC substrate oscillating at 13.8 kHz deforms ∼3 times less than traditional optical glasses, and 2.6 times less than Clearceram-Z resonating at 15.1 kHz [23], reaching values comparable to beryllium but without the high costs due to its toxicity during the manufacturing process. Further, SiC composites exhibit greater thermal stability than beryllium [28]. The small dynamic distortion of the MEMS scanner (Fig. 5) offers a promising alternative to galvanometric resonant scanners, with diffraction-limited performance over comparable Lagrange invariants to those of galvanometric scanners and currently unattainably high resonant frequencies.

In summary, the use of both the SiC substrate and the MEMS scanners can improve the performance of imaging and sensing instrumentation that requires mechanical beam deflection through resonant scanners.

Funding. Research to Prevent Blindness (Challenge Grant); National Eye Institute (P30EY026877, R01EY025231, R01EY028287, R01EY031360, R01EY032147, R01EY032669).

Acknowledgment. The resonant scanner tested in this work was kindly loaned to the authors by Hamamatsu Corporation. We thank Mario Kasahara, Hamamatsu, for providing the finite-element analysis data and the MEMS scanner unit used in this work.

Disclosures. The authors declare no conflicts of interest.

Data Availability. Data underlying the results presented in this paper are not publicly available at this time but may be obtained from the authors upon reasonable request.

REFERENCES

1. M. G. Giacomelli, Y. Sheikine, H. Vardeh, J. L. Connolly, and J. G. Fujimoto, "Rapid imaging of surgical breast excisions using direct temporal sampling two photon fluorescent lifetime imaging," Biomed. Opt. Express **6**, 4317–4325 (2015).
2. R. Y. Tsien and B. J. Bacskai, "Video-rate confocal microscopy," in *Handbook of Biological Confocal Microscopy*, J. B. Pawley, ed. (Springer, 1995), pp. 459–478.
3. Y. Ozeki, W. Umemura, Y. Otsuka, S. Satoh, H. Hashimoto, K. Sumimura, N. Nishizawa, K. Fukui, and K. Itoh, "High-speed molecular spectral imaging of tissue with stimulated Raman scattering," Nat. Photonics **6**, 845–851 (2012).
4. F. Bottanelli, E. B. Kromann, E. S. Allgeyer, R. S. Erdmann, S. Wood Baguley, G. Sirinakis, A. Schepartz, D. Baddeley, D. K. Toomre, J. E. Rothman, and J. Bewersdorf, "Two-colour live-cell nanoscale imaging of intracellular targets," Nat. Commun. **7**, 10778 (2016).
5. R. H. Webb, G. W. Hughes, and O. Pomerantzeff, "Flying spot TV ophthalmoscope," Appl. Opt. **19**, 2991–2997 (1980).
6. A. Roorda, F. Romero-Borja, W. Donnelly, III, H. Queener, T. Hebert, and M. Campbell, "Adaptive optics scanning laser ophthalmoscopy," Opt. Express **10**, 405–412 (2002).
7. A. Dubra and Y. Sulai, "Reflective afocal broadband adaptive optics scanning ophthalmoscope," Biomed. Opt. Express **2**, 1757–1768 (2011).
8. A. M. Rollins, M. D. Kulkarni, S. Yazdanfar, R. Ung-arunyawee, and J. A. Izatt, "In vivo video rate optical coherence tomography," Opt. Express **3**, 219–229 (1998).
9. W. Wieser, W. Draxinger, T. Klein, S. Karpf, T. Pfeiffer, and R. Huber, "High definition live 3D-OCT in vivo: design and evaluation of a 4D OCT engine with 1 GVoxel/s," Biomed. Opt. Express **5**, 2963–2977 (2014).
10. T. J. Kulp, D. Garvis, R. Kennedy, T. Salmon, and K. Cooper, "Development and testing of a synchronous-scanning underwater imaging system capable of rapid two-dimensional frame imaging," Appl. Opt. **32**, 3520–3530 (1993).
11. K. Hiramatsu, T. Ideguchi, Y. Yonamine, S. Lee, Y. Luo, K. Hashimoto, T. Ito, M. Hase, J.-W. Park, Y. Kasai, S. Sakuma, T. Hayakawa, F. Arai, Y. Hoshino, and K. Goda, "High-throughput label-free molecular fingerprinting flow cytometry," Sci. Adv. **5**, eaau0241 (2019).
12. J. C. Urbach, T. S. Fisli, and G. K. Starkweather, "Laser scanning for electronic printing," Proc. IEEE **70**, 597–618 (1982).
13. B. W. Pearre, C. Michas, J.-M. Tsang, T. J. Gardner, and T. M. Otchy, "Fast micron-scale 3D printing with a resonant-scanning two-photon microscope," Addit. Manuf. **30**, 100887 (2019).
14. P. J. Brosens, "Dynamic mirror distortions in optical scanning," Appl. Opt. **11**, 2987–2989 (1972).
15. R. A. Conant, J. T. Nee, K. Y. Lau, and R. S. Muller, "Dynamic deformation of scanning mirrors," in *IEEE/LEOS International Conference on Optical MEMS* (IEEE, 2000), pp. 49–50.
16. S. Hsu, T. Klose, C. Drabe, and H. Schenk, "Fabrication and characterization of a dynamically flat high resolution micro-scanner," J. Opt. **10**, 044005 (2008).
17. U. Hofmann, J. Janes, and H.-J. Quenzer, "High-Q MEMS resonators for laser beam scanning displays," Micromachines **3**, 509–528 (2012).
18. A. R. Cho, A. Han, S. Ju, H. Jeong, J.-H. Park, I. Kim, J.-U. Bu, and C.-H. Ji, "Electromagnetic biaxial microscanner with mechanical amplification at resonance," Opt. Express **23**, 16792–16802 (2015).
19. R. Farrugia, I. Grech, D. Camilleri, O. Casha, E. Gatt, and J. Micallef, "Theoretical and finite element analysis of dynamic deformation in resonating micromirrors," Microsyst. Technol. **24**, 445–455 (2018).
20. M. Brown, T. Gong, D. Neal, J. Roller, S. Luanava, and H. Urey, "Measurement of the dynamic deformation of a high-frequency scanning mirror using a Shack-Hartmann wavefront sensor," Proc. SPIE **4451**, 480–488 (2001).
21. M. R. Hart, R. A. Conant, K. Y. Lau, and R. S. Muller, "Stroboscopic interferometer system for dynamic MEMS characterization," J. Microelectromech. Syst. **9**, 409–418 (2000).
22. H. Urey, D. Wine, and T. Osborn, "Optical performance requirements for MEMS-scanner-based microdisplays," Proc. SPIE **4178**, 176–185 (2000).
23. V. Akondi, B. Kowalski, S. A. Burns, and A. Dubra, "Dynamic distortion in resonant galvanometric optical scanners," Optica **7**, 1506–1513 (2020).
24. optoSiC, 2021, https://optosic.de/product-overview.html.
25. Entegris Inc., 2021, https://entegris.com/en/home/products/specialty-materials/premium-silicon-carbide.html.
26. Advanced Mechanical and Optical Systems (AMOS), 2021, https://amos.be/technology/mirrors.
27. Aperture Optical Sciences Inc., 2021, https://apertureos.com/products/sic-optics.
28. D. A. Bath and E. A. Ness, "Applying silicon carbide to optics," Opt. Photon. News **19**(5), 10–13 (2008).
29. R. Cooper and A. Harrison, "The uses and adverse effects of beryllium on health," Indian J. Occup. Environ. Med. **13**, 65–76 (2009).
30. S. Kurth, C. Kaufmann, R. Hahn, J. Mehner, W. Doetzel, and T. Gessner, "A novel 24-kHz resonant scanner for high-resolution laser display," Proc. SPIE **5721**, 23–33 (2005).
31. U. Baran, D. Brown, S. Holmstrom, D. Balma, W. O. Davis, A. Mazzalai, P. Muralt, and H. Urey, "High frequency torsional MEMS

scanner for displays," in *IEEE International Conference on Micro Electro Mechanical Systems* (IEEE, 2012), pp. 636–639.
32. S. T. S. Holmström, U. Baran, and H. Urey, "MEMS laser scanners: a review," J. Microelectromech. Syst. **23**, 259–275 (2014).
33. D. Wang, C. Watkins, and H. Xie, "MEMS mirrors for LiDAR: a review," Micromachines **11**, 456 (2020).
34. H. Miyajima, N. Asaoka, T. Isokawa, M. Ogata, Y. Aoki, M. Imai, O. Fujimori, M. Katashiro, and K. Matsumoto, "A MEMS electromagnetic optical scanner for a commercial confocal laser scanning microscope," J. Microelectromech. Syst. **12**, 243–251 (2003).
35. H. Miyajima, "Development of a MEMS electromagnetic optical scanner for a commercial laser scanning microscope," J. Microelectromech. Syst. **3**, 243–251 (2004).
36. H. Miyajima, K. Murakami, and M. Katashiro, "MEMS optical scanners for microscopes," IEEE J. Sel. Top. Quantum Electron. **10**, 514–527 (2004).
37. K. C. Maitland, H. J. Shin, H. Ra, D. Lee, O. Solgaard, and R. Richards-Kortum, "Single fiber confocal microscope with a two-axis gimbaled MEMS scanner for cellular imaging," Opt. Express **14**, 8604–8612 (2006).
38. C. L. Arrasmith, D. L. Dickensheets, and A. Mahadevan-Jansen, "MEMS-based handheld confocal microscope for in-vivo skin imaging," Opt. Express **18**, 3805–3819 (2010).
39. D. L. Dickensheets and G. S. Kino, "Micromachined scanning confocal optical microscope," Opt. Lett. **21**, 764–766 (1996).
40. H.-J. Shin, M. C. Pierce, D. Lee, H. Ra, O. Solgaard, and R. Richards-Kortum, "Fiber-optic confocal microscope using a MEMS scanner and miniature objective lens," Opt. Express **15**, 9113–9122 (2007).
41. H. Ra, W. Piyawattanametha, Y. Taguchi, D. Lee, M. J. Mandella, and O. Solgaard, "Two-dimensional MEMS scanner for dual-axes confocal microscopy," J. Microelectromech. Syst. **16**, 969–976 (2007).
42. E. C. M. Disseldorp, F. C. Tabak, A. J. Katan, M. B. S. Hesselberth, T. H. Oosterkamp, J. W. M. Frenken, and W. M. V. Spengen, "MEMS-based high speed scanning probe microscopy," Rev. Sci. Instrum. **81**, 043702 (2010).
43. A. Cogliati, C. Canavesi, A. Hayes, P. Tankam, V.-F. Duma, A. Santhanam, K. P. Thompson, and J. P. Rolland, "MEMS-based handheld scanning probe with pre-shaped input signals for distortion-free images in Gabor-domain optical coherence microscopy," Opt. Express **24**, 13365–13374 (2016).
44. H. Urey, "Torsional MEMS scanner design for high-resolution scanning display systems," Proc. SPIE **4773**, 27–37 (2002).
45. A. D. Yalcinkaya, H. Urey, D. Brown, T. Montague, and R. Sprague, "Two-axis electromagnetic microscanner for high resolution displays," J. Microelectromech. Syst. **15**, 786–794 (2006).
46. U. Baran, D. Brown, S. Holmstrom, D. Balma, W. O. Davis, P. Muralt, and H. Urey, "Resonant PZT MEMS scanner for high-resolution displays," J. Microelectromech. Syst. **21**, 1303–1310 (2012).
47. U. Hofmann, F. Senger, F. Soerensen, V. Stenchly, B. Jensen, and J. Janes, "Biaxial resonant 7mm-MEMS mirror for automotive LIDAR application," in *IEEE/LEOS International Conference on Optical MEMS* (IEEE, 2012), pp. 150–151.
48. H. W. Yoo, N. Druml, D. Brunner, C. Schwarzl, T. Thurner, M. Hennecke, and G. Schitter, "MEMS-based lidar for autonomous driving," Elektrotech. Inftech. **135**, 408–415 (2018).
49. F. Schwarz, F. Senger, J. Albers, P. Malaurie, C. Janicke, L. Pohl, F. Heinrich, D. Kaden, H.-J. Quenzer, F. Lofink, A. Bahr, T. von Wantoch, and U. Hofmann, "Resonant 1D MEMS mirror with a total optical scan angle of 180° for automotive LiDAR," Proc. SPIE **11293**, 1129309 (2020).
50. A. Wolter, H. Schenk, E. Gaumont, and H. Lakner, "MEMS microscanning mirror for barcode reading: from development to production," Proc. SPIE **5348**, 32–39 (2004).
51. A. D. Yalcinkaya, O. Ergeneman, and H. Urey, "Polymer magnetic scanners for bar code applications," Sens. Actuators A **135**, 236–243 (2007).
52. F. Woittennek, J. Knobbe, T. Pügner, H.-G. Dallmann, U. Schelinski, and H. Grüger, "MEMS scanner mirror based system for retina scanning and in eye projection," Proc. SPIE **9375**, 937506 (2015).
53. J. Lee, S. Moon, J. Lim, M.-J. Gwak, J. G. Kim, E. Chung, and J.-H. Lee, "Imaging of the finger vein and blood flow for anti-spoofing authentication using a laser and a MEMS scanner," Sensors **17**, 925 (2017).
54. V. Akondi and A. Dubra, "Accounting for focal shift in the Shack–Hartmann wavefront sensor," Opt. Lett. **44**, 4151–4154 (2019).
55. L. D. S. Haro and J. C. Dainty, "Single vs asymmetric double-pass measurement of the wavefront aberration of the human eye," in *Vision Science and Its Applications*, OSA Technical Digest Series (Optical Society of America, 1999), paper SuC1.
56. V. Akondi and A. Dubra, "Average gradient of Zernike polynomials over polygons," Opt. Express **28**, 18876–18886 (2020).
57. W. H. Southwell, "Wave-front estimation from wave-front slope measurements," J. Opt. Soc. Am. **70**, 998–1006 (1980).
58. V. Akondi, S. Steven, and A. Dubra, "Centroid error due to non-uniform lenslet illumination in the Shack–Hartmann wavefront sensor," Opt. Lett. **44**, 4167–4170 (2019).
59. J. W. Goodman, *Introduction to Fourier Optics*, 4th ed. (W. H. Freeman and Company, 2017).
60. X. Huang and A. Dubra, "Correction of resonant optical scanner dynamic aberrations using nodal aberration theory," Opt. Express **29**, 10346–10363 (2021).
61. L. N. Thibos, R. A. Applegate, J. T. Schwiegerling, and R. Webb, "Standards for reporting the optical aberrations of eyes," J. Refract. Surg. **18**, S652–S660 (2002).
62. C. Tischbirek, A. Birkner, H. Jia, B. Sakmann, and A. Konnerth, "Deep two-photon brain imaging with a red-shifted fluorometric Ca^{2+} indicator," Proc. Natl. Acad. Sci. USA **112**, 11377 (2015).
63. N. T. Urban, K. I. Willig, S. W. Hell, and U. V. Nägerl, "STED nanoscopy of actin dynamics in synapses deep inside living brain slices," Biophys. J. **101**, 1277–1284 (2011).
64. S. Weisenburger, F. Tejera, J. Demas, B. Chen, J. Manley, F. T. Sparks, F. Martínez Traub, T. Daigle, H. Zeng, A. Losonczy, and A. Vaziri, "Volumetric Ca^{2+} imaging in the mouse brain using hybrid multiplexed sculpted light microscopy," Cell **177**, 1050–1066 (2019).

37.119.162.182 {ts '2021-12-21 08:33:26'}